Intermetallics 155 (2023) 107846

Contents lists available at ScienceDirect

Intermetallics

journal homepage: www.elsevier.com/locate/intermet

Core-shell structure and stability of nanocrystalline precipitates in $Fe_{83.3}Si_4B_8P_4Cu_{0.7}$ soft magnetic amorphous alloy

Chenyu Lu [a], Jiacheng Ge [b], Si Lan [a,b], Xuelian Wu [a], Zhenduo Wu [c], Lingxiang Shi [a,c], Anding Wang [d], Yan Zhang [e], Chi Long Lai [a], Kit Ying Leung [a], Junhua Luan [f], Elliot Paul Gilbert [g], Xun-Li Wang [a,h,i,*]

[a] Department of Physics, City University of Hong Kong, Hong Kong, China
[b] Herbert Gleiter Institute of Nanoscience, School of Materials Science and Engineering, Nanjing University of Science and Technology, Nanjing, 210094, China
[c] City University of Hong Kong (Dongguan), Dongguan, 523000, China
[d] School of Materials Science and Engineering, Dongguan University of Technology, Dongguan, 523808, China
[e] Ningbo Institute of Materials Technology and Engineering, Chinese Academy of Sciences, Ningbo, 315201, China
[f] Department of Materials Science and Engineering, City University of Hong Kong, Hong Kong, China
[g] Australian Centre for Neutron Scattering, Australian Nuclear Science and Technology Organization, Lucas Heights, New South Wales, 2234, Australia
[h] Center for Neutron Scattering, City University of Hong Kong, Hong Kong, China
[i] City University of Hong Kong Shenzhen Research Institute, Shenzhen, 518057, China

ARTICLE INFO

Keywords:
Amorphous/nanocrystalline alloys
Nanocrystalline structure
Thermal stability
Atom probe

ABSTRACT

The core-shell nanostructure of α-Fe precipitates was investigated in a recently developed high-performance $Fe_{83.3}Si_4B_8P_4Cu_{0.7}$ nanocrystalline soft magnetic alloy utilizing small-angle neutron scattering (SANS) and atom probe tomography (APT). SANS measurements under a saturating magnetic field provided evidence of core-shell structures at the nanoscale. Moreover, the core-shell structure was directly visualized from APT analysis, where P-enriched shells were found around Fe-enriched cores due to the large negative heat of mixing between Fe and P elements and the slow diffusion of P atoms. The core-shell nanostructures induced by nanoscale partitioning are effective in stabilizing the residual amorphous matrix and suppressing the crystal growth. Our findings provide insight into the microstructure of Fe-based amorphous alloys and have direct implications in alloy design for the improvement of the soft magnetic properties.

1. Introduction

Fe-based nanocrystalline soft magnetic alloys, normally obtained by thermal annealing of amorphous precursors, have attracted increasing attention as promising materials in the field of energy transmission and conversion due to their excellent soft magnetic properties [1–4]. The saturation magnetic flux density (B_s) and coercivity (H_c) are two important parameters. Thus, improving B_s and reducing H_c have been the long-term goals for improved performance of soft magnetic materials. It is generally known that H_c decreases with the sixth power of the grain size according to the random anisotropy model [2]. Therefore, understanding the mechanism of nanoscale crystallization is essential to obtaining a uniform microstructure of fine α-Fe grains for the improvement of soft magnetic properties.

As a well-developed soft magnetic alloy, Fe–Si–B–Nb–Cu (FINEMET) [5] has been systematically investigated for the crystallization mechanism utilizing transmission electron microscopy (TEM) [6], atom probe tomography (APT) [7] and small-angle neutron scattering (SANS) [8,9]. Earlier studies have demonstrated solute clustering and partitioning behavior in the early crystallization of FINEMET [6], where the Fe_3Si type nanocrystals were surrounded by an Nb-enriched shell [9]. Hence, the large Nb atoms appeared to serve as pinning sites, which constrained the coarsening of the nanoscale precipitates thereby stabilizing the nanostructure.

To reduce the production cost and further improve the soft magnetic properties, other alloy systems have been developed by increasing the Fe concentration and replacing transition metal elements with metalloid elements, such as in Fe–B–C–Cu [10], Fe–P–C–Cu [11], Fe–Si–B–P–C [12], and Fe–Si–B–P–C–Cu [13]. The recently developed Fe–Si–B–P–Cu (NANOMET type) alloys were reported to exhibit a superior saturation

* Corresponding author. Department of Physics, City University of Hong Kong, Hong Kong, China.
E-mail address: xlwang@cityu.edu.hk (X.-L. Wang).

https://doi.org/10.1016/j.intermet.2023.107846
Received 30 November 2022; Received in revised form 18 January 2023; Accepted 25 January 2023
Available online 27 January 2023

magnetic flux density up to 1.88 T, comparable to that of Si steels, accompanied by one-third lower core loss at 50 Hz [14]. The significant differences between the FINEMET and NANOMET type alloys are the increase of Fe concentration and the replacement of Nb atoms by the smaller P atoms. It is anticipated that P would play a crucial role in stabilizing nanoscale precipitates during the annealing process. It has been shown that the addition of P can hinder the growth of α-Fe precipitates and also slow down the crystallization of the residual amorphous phase [15]; however, the underlying mechanism has not been established. Recently, a transient metalloid-rich shell structure around the α-Fe(Si) precipitates was found in short-time annealed Fe–Si–B–P–C samples based on APT analysis [16]. Nevertheless, the formation and effects of core-shell structures on the magnetic properties after long-time annealing are not well understood. In this regard, experimental investigation from significant numbers of precipitates in a bulk sample is needed to establish the core-shell structure and understand its formation and stabilization mechanism. SANS is a powerful tool to characterize the size, size distribution, morphology and volume fraction of nanoscale precipitates in bulk samples. In this study, we applied a combination of state-of-the-art characterization techniques, including SANS and APT, to directly investigate the formation of the core-shell nanostructure of precipitates in the $Fe_{83.3}Si_4B_8P_4Cu_{0.7}$ soft magnetic alloy after different heat treatments. This work sheds light on the mechanism of nanoscale precipitation and helps guide the development of soft magnetic materials for a wide range of applications.

2. Experimental procedures

A multi-component alloy with a nominal composition of $Fe_{83.3}Si_4B_8P_4Cu_{0.7}$ (at.%) was prepared by induction melting with the mixture of pure Fe (99.98 mass%), Si (99.998 mass%), B (99.5 mass%), Cu (99.99 mass%) and pre-alloyed Fe_3P (99.5 mass%) in an Ar atmosphere. The master alloy was then used to prepare amorphous ribbons with a width of about 10 mm and a thickness of about 20 μm via the single-roller melt-spinning method. The thermal properties of the as-quenched ribbons were evaluated using differential scanning calorimetry (DSC, NETZSCH 404C) with a constant heating rate of 40 °C/min under a high purity Ar atmosphere. The SANS experiments were carried out on the QUOKKA instrument at the OPAL reactor at ANSTO, Australia, to study the nanoscale precipitates in $Fe_{83.3}Si_4B_8P_4Cu_{0.7}$ soft magnetic alloys annealed at 350 and 380 °C for different annealing times [17]. Isothermal annealing was pre-performed with a high vacuum tube furnace followed by water quenching to synthesize nanocrystalline alloys. The annealed ribbon samples were prepared and stacked together to a thickness of about 0.5 mm for SANS measurements. To separate the contributions from nuclear and magnetic scattering, a saturating magnetic field of 2 T was applied in the scattering plane normal to the incident neutron beam direction. The beam size was 5 mm in diameter, and the wavelength of the incident neutrons was 5 Å with a resolution of 10%. Three instrument configurations with different source-to-sample distances (SSDs) and sample-to-detector distances (SDDs) were employed to cover a wide range of scattering vector Q from 0.004 to 0.7 $Å^{-1}$ ($Q = 4\pi \sin\theta/\lambda$, where λ is the wavelength and 2θ is the scattering angle). SANS data were reduced and analyzed using NCNR SANS reduction and analysis macros modified for the QUOKKA instrument installed in Igor software (Wavemetrics) [18]. One-dimensional scattering cross-sections were obtained by azimuthal averaging over ± 15° around the parallel and perpendicular directions to the applied magnetic field. The APT characterizations were conducted in a CAMEACA LEAP 5000 R instrument. Needle-shaped specimens for APT were fabricated using an FEI Scios focused ion beam/scanning electron microscope (FIB/SEM). The three-dimensional data reconstructions and analysis were performed using Image Visualization and Analysis Software (IVAS) version 3.8.

3. Results and discussion

Fig. 1 shows the DSC curve for the $Fe_{83.3}Si_4B_8P_4Cu_{0.7}$ amorphous alloy at a heating rate of 40 °C/min. Two exothermic crystallization peaks are well-separated, representing the formation of α-Fe precipitates and compounds, respectively [19]. The onset temperatures of primary crystallization (T_{x1}) and secondary crystallization (T_{x2}) are determined and marked with black arrows. The interval of crystallization temperatures ΔT_x ($\Delta T_x = T_{x2}$-T_{x1}) exhibits a large value of about 140 °C, which favors the formation of stable α-Fe grains without other compounds over a wide range of annealing temperatures [16]. Based on these DSC results, two different annealing temperatures below the primary crystallization temperature, 350 and 380 °C, were chosen as indicated by black arrows with T_{a1} and T_{a2}, for the following SANS and APT characterizations.

The crystallization behavior and soft magnetic properties of the NANOMET alloys are sensitively dependent on the annealing temperature [20] and annealing time [21]. SANS is a powerful technique to unveil the precipitation mechanisms at the nanoscale, particularly well adapted to the study of ferromagnetic materials [22–24]. By applying a saturating magnetic field of 2 T, the magnetic moments are aligned along the applied magnetic field direction. As a result, the magnetic contribution should be zero in the field direction and maximum in the perpendicular direction (see below). A representative two-dimensional SANS pattern is observed, as shown in Fig. 2(a). Under the saturating magnetic field, the total scattering cross-section $\frac{d\Sigma}{d\Omega}(Q)$ can be obtained from SANS patterns and be expressed by Ref. [25]:

$$\frac{d\Sigma}{d\Omega}(Q) = \left(\frac{d\Sigma}{d\Omega}\right)_{nuc} + \left(\frac{d\Sigma}{d\Omega}\right)_{mag} \sin^2\alpha \quad (1)$$

where α is the angle between the scattering vector Q and the applied magnetic field. The scattering intensities in the parallel ($\alpha = 0°$) and perpendicular ($\alpha = 90°$) directions to the applied magnetic field are depicted with $\left(\frac{d\Sigma}{d\Omega}\right)_{H\|Q}$ and $\left(\frac{d\Sigma}{d\Omega}\right)_{H\perp Q}$, respectively. Thus, the isotropic nuclear and anisotropic magnetic scattering are simplified to:

$$\left(\frac{d\Sigma}{d\Omega}\right)_{nuc} = \left(\frac{d\Sigma}{d\Omega}\right)_{H\|Q} \quad (2)$$

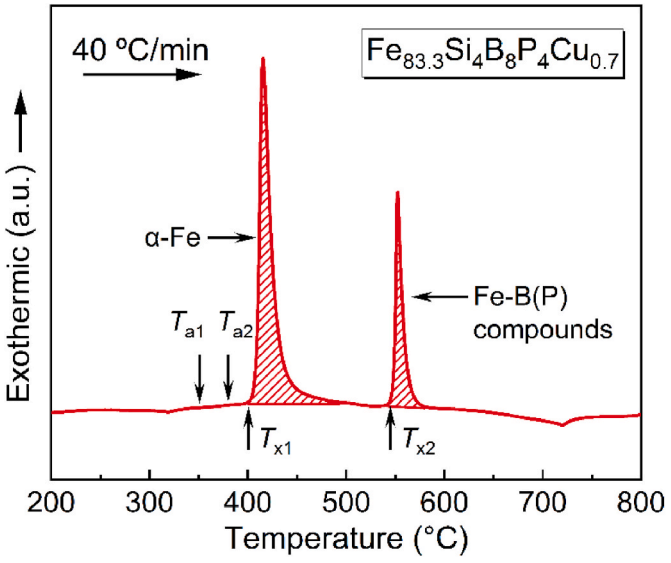

Fig. 1. The DSC curve for $Fe_{83.3}Si_4B_8P_4Cu_{0.7}$ amorphous alloy at a heating rate of 40 °C/min, showing two well-separated crystallization peaks. Crystallization temperatures (T_{x1} and T_{x2}) and annealing temperatures (T_{a1} and T_{a2}) are indicated by black arrows.

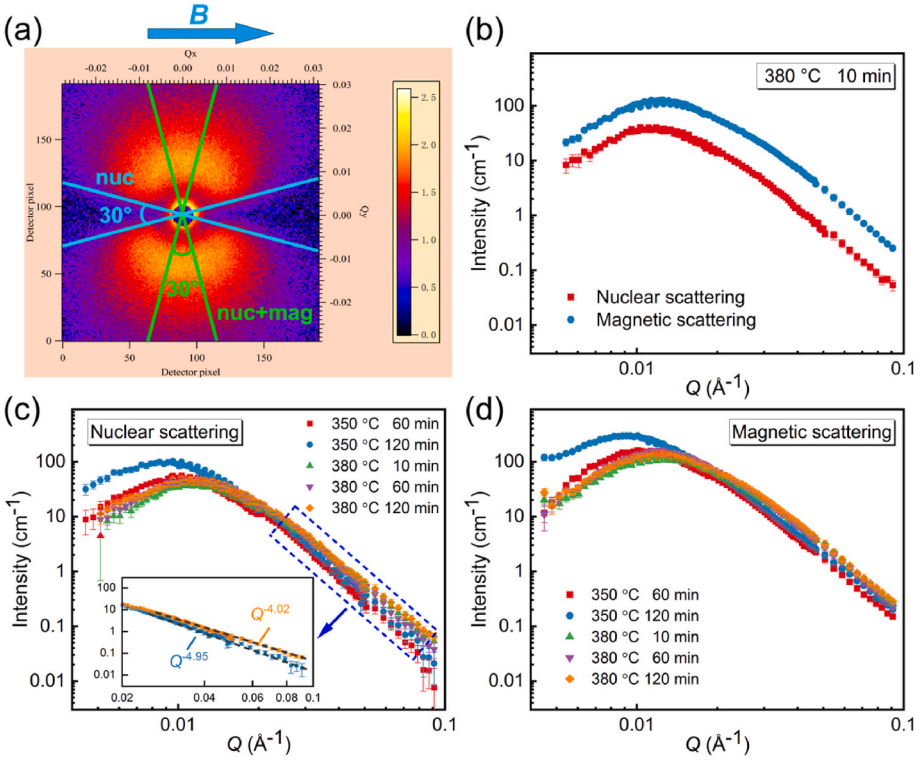

Fig. 2. SANS results under a horizontal magnetic field of 2 T. (a) Anisotropic two-dimensional SANS pattern. (b) The comparison of the nuclear and magnetic scattering for the sample annealed at 380 °C for 10 min. (c) Nuclear and (d) magnetic SANS scattering intensity versus scattering vector Q for $Fe_{83.3}Si_4B_8P_4Cu_{0.7}$ samples annealed at 350 and 380 °C for different times. The inset in (c) shows the fitted power-law.

$$\left(\frac{d\Sigma}{d\Omega}\right)_{mag} = \left(\frac{d\Sigma}{d\Omega}\right)_{H\perp Q} - \left(\frac{d\Sigma}{d\Omega}\right)_{H\parallel Q} \quad (3)$$

For clarity, the nuclear and magnetic scattering as a function of Q can be well extracted individually from the two-dimensional pattern using sectors with an azimuthal angle of 30° and are compared in Fig. 2(b). The magnetic and nuclear scattering are respectively from the magnetic and nuclear contrast between precipitates and the amorphous matrix, which accounts for the similar trends in both scattering profiles. Fig. 2(c) and (d) show the Q dependence of nuclear and magnetic scattering components for samples annealed at 350 and 380 °C for different annealing times. To extract the scattering of precipitation due to annealing, the intensity of the as-quenched sample has been subtracted as weak background from all cases [25]. In the dilute system, the SANS intensities show interference peaks that are dependent on the annealing temperature and annealing time for both nuclear and magnetic scattering. With increasing annealing time, the SANS intensity becomes more pronounced, and the interference peak shifts to lower Q, which indicates that larger particles are formed at 350 °C. In contrast, at 380 °C, it appears that the SANS intensities remain stable with increasing annealing time.

The sizes of the scattering particles can be estimated by the Guinier approximation at the low Q region of SANS data by the following equation [26,27]:

$$I(Q) \propto \exp\left(-\frac{R_g^2 Q^2}{3}\right) \quad (4)$$

where R_g is the radius of gyration. Here, for spherical precipitates, the average radius R is given by $R = \sqrt{5/3}\, R_g$. Using this approach, the average particle sizes were evaluated for different samples and the results are summarized in Table 1. It can be seen that the nanocrystalline particles continued to grow for 120 min at 350 °C, whereas the particles reached a growth plateau and became stable after just 10 min at 380 °C.

Table 1
Particle sizes calculated by the Guinier approximation of SANS nuclear scattering intensities for $Fe_{83.3}Si_4B_8P_4Cu_{0.7}$ samples after annealing at different conditions.

Sample	350 °C		380 °C		
	60 min	120 min	10 min	60 min	120 min
Particle size (nm)	32.5 ± 0.3	37.0 ± 0.3	27.7 ± 0.6	29.1 ± 0.4	29.6 ± 0.3

The average sizes of precipitates remained nearly stable, even after prolonged annealing for 120 min at 380 °C, suggesting that the particle sizes reached saturation and stable state after a short annealing time at higher annealing temperature, which is consistent with previous reports [28]. Meanwhile, the power-law scattering ($I(Q) \propto Q^{-n}$) can be applied to the nuclear scattering intensity, as shown by the dashed lines in the inset of Fig. 2(c) [29]. The fitted power-law exponents n, ranging from 4.02 to 4.95, are all larger than 4, which indicates that there are diffuse boundaries between the matrix and crystalline particles [30,31]. The appearance of interference peaks can be attributed to core-shell nanostructures in a dilute system [32]. Indeed, interference peaks produced by core-shell structures have also been observed by small-angle scattering in many other amorphous alloys, e.g., Zr-based [32], Mg-based [33] and Fe-based [9], indicating that the core-shell nanostructure might be a common characteristic of crystalline precipitates in the matrix.

To further substantiate the core-shell nanostructure, composition fluctuations were detected by APT on nanocrystalline samples annealed at 350 and 380 °C for 60 min. Elemental segregation is clearly seen, as shown in Fig. 3(a)-(c). Cu-clusters with a high number density of 10^{24} m^{-3} are observed, which is attributable to the immiscibility of Cu in the Fe-based matrix. The high Cu-containing clusters can serve as preferential heterogeneous nucleation sites as previously pointed out by Hono

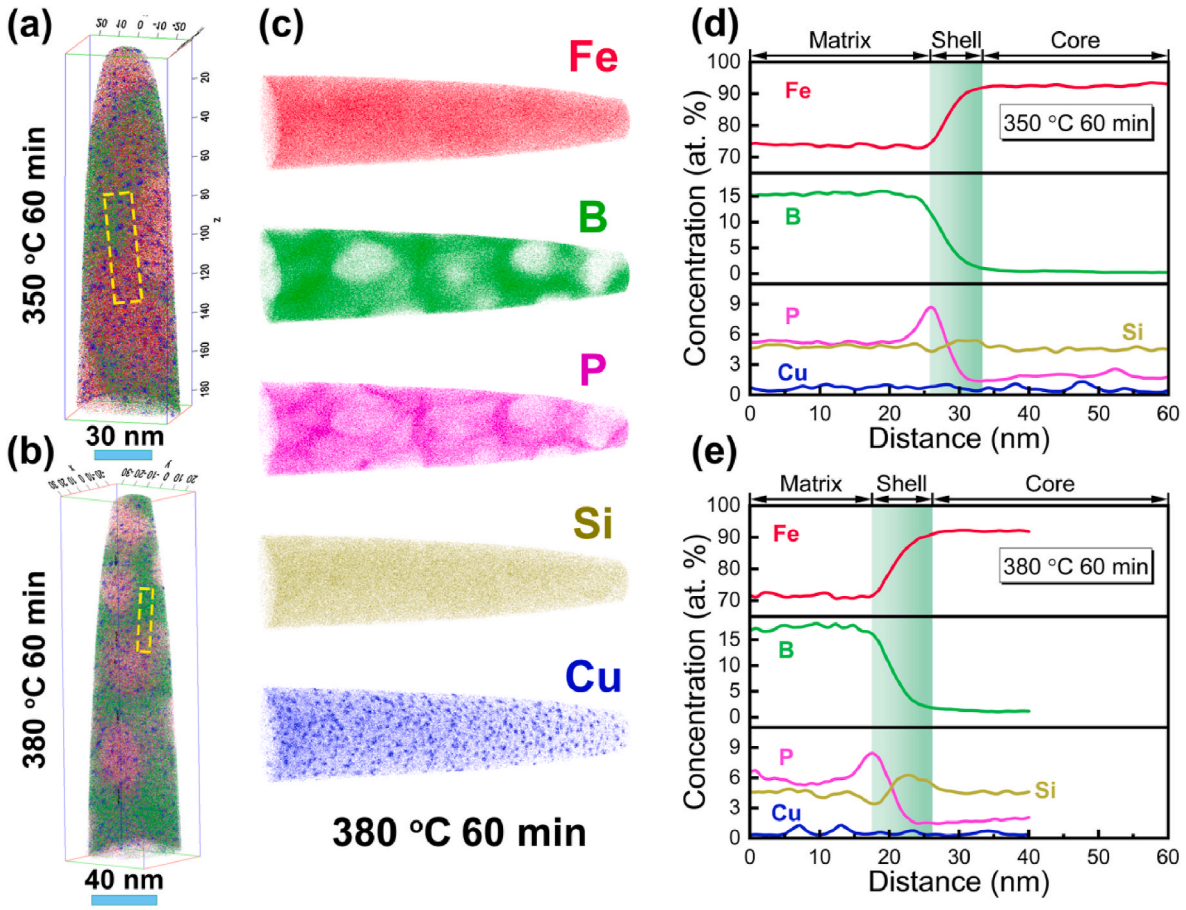

Fig. 3. APT elemental maps of $Fe_{83.3}Si_4B_8P_4Cu_{0.7}$ alloys annealed at (a) 350 °C (53 ×53 × 188 nm) and (b) 380 °C (60 ×60 × 232 nm) for 60 min. (c) APT elemental maps for constituent Fe, B, P, Si, and Cu, respectively, for the sample annealed at 380 °C for 60 min. (d–e) Concentration depth profiles from the selected dashed area shown in (a–b), respectively.

et al. in FINEMET alloys [6]. Fig. 3(d) and (e) present the concentration depth profiles across the precipitate/matrix interface from the selected dashed areas as illustrated in Fig. 3(a)–(b). The region is divided into three parts consisting of Fe-enriched core, P-enriched shell, and amorphous matrix based on composition variations. It is evident that Fe elements are enriched in the cores of grains with a concentration of up to 90 at.%. The Si elements are dissolved in both Fe-enriched core and amorphous matrix and show a slight variation in the shell. The metalloid elements of B and P are rejected from the Fe-enriched cores towards the surrounding matrix. The B concentration shows a normal gradual rising trend from the core of precipitates to the matrix. Interestingly, there is an apparent enhancement of P concentration between precipitates and amorphous matrix in both cases.

In order to understand the reason for the P enrichment, the heat of mixing among the constituent elements, compiled in Table 2, is considered [34]. It is noteworthy that Cu atoms tend to segregate to Cu clusters prior to crystallization owing to the positive heat of mixing between Fe and Cu elements [35]. These Cu clusters could stimulate the nucleation of α-Fe nanograins by reducing the activation energy [7]. When α-Fe crystalline particles heterogeneously nucleate at the sites of Cu clusters from the amorphous matrix, P and B atoms are excluded from the α-Fe crystalline phase because their solubility limits are virtually zero below 400 °C [36]. Consequently, the residual amorphous phase becomes enriched in P and B atoms, which increases the stability of the amorphous matrix. Fe–P also has the largest negative heat of mixing, and therefore the strongest attractive interactions [32]. Correspondingly, the strong attractive interactions can provide a driving force for Fe-enriched cores to attract P atoms in the amorphous matrix and promote the enhanced P concentration in the surrounding shell. Besides, the growth of precipitates depends on the diffusion of constituent atoms. Different diffusion rates of the metalloids are also responsible for the P enrichment. Indeed, the atomic radius of P (0.109 nm) is much larger than that of B (0.09 nm) [37,38]. Simulation has suggested that larger P atoms exhibit a much lower diffusion ability than B atoms [39]. During the formation of α-Fe precipitates, B atoms are redistributed quickly in the matrix because of their high diffusion rate, which would hardly inhibit the growth of precipitates. While the formation of α-Fe precipitates has to push P atoms out of the precipitates, the relatively slow diffusion ability of P elements limits its expulsion to the matrix and eventually leads to the enrichment of P around precipitates.

When taken together, the combination of SANS and APT provides direct evidence of nanoscale core-shell structures of α-Fe precipitates in the $Fe_{83.3}Si_4B_8P_4Cu_{0.7}$ amorphous alloy. SANS profiles are characterized by prominent interference peaks, which is a signature of core-shell

Table 2
Heat of mixing (kJ mol^{-1}) for constituent elements in the $Fe_{83.3}Si_4B_8P_4Cu_{0.7}$ amorphous alloy [34,35].

Elements	Fe–P	Fe–Si	Fe–B	Si–P	Si–Cu	Cu–P	Si–B	Cu–B	B–P	Fe–Cu
Heat of mixing (kJ mol^{-1})	−39.5	−35	−26	−25.5	−19	−17.5	−14	0	0.5	13

structures with diffusion zones [32]. Power-law-scattering exponents calculated from the nuclear scattering are greater than 4 in all cases, implying the formation of diffuse boundaries between precipitates and matrix. Furthermore, APT results show composition fluctuations and reveal P-enriched shells around Fe-enriched cores. During crystallization, the P-rich shells act as a diffusion barrier and severely restrict the mobilities of solute elements like B, Cu and Si in the amorphous matrix. Hence, the kinetics of solute partitioning becomes slower. The existence of P enrichments is effective in stabilizing the remaining amorphous phase and hampers the crystal growth. Moreover, the thickness of the shell region appeared to increase with the annealing temperature as shown in Fig. 3(d) and (e). At higher annealing temperatures, the thicker shell can make the diffusion of Fe atoms from the matrix into crystals more difficult and can play a more significant role in suppressing the crystal growth. This can explain the stability of the precipitates for samples annealed at 380 °C, where the particle sizes do not continue to grow after just 10 min and remain stable even for 120 min. Hence, the core-shell nanostructures play an important role in the stability of nanocrystalline precipitates and can also be helpful for the improvement of soft magnetic properties, opening the possibility for further soft magentic material development.

4. Conclusions

In summary, through a combination of SANS under a saturating magnetic field and APT, we investigated the core-shell nanostructure of α-Fe precipitates in a recently developed $Fe_{83.3}Si_4B_8P_4Cu_{0.7}$ soft magnetic amorphous alloy at the nanoscale. The SANS profiles display a characteristic interference peak, as well as a power-law exponent greater than four, both of which can be attributed to the core-shell structures. In addition, APT compositional profiles reveal a prominent P-enriched shell surrounding the Fe-enriched core. The core-shell structures are formed because of nanoscale partitioning, where the slow diffusion of P atoms and the strong attractive interactions between P and Fe elements give rise to the P enrichment. Consequently, it becomes difficult for α-Fe grains to grow continuously because the diffusion of Fe atoms from the amorphous matrix into grains is effectively impeded by P-enriched shells. These experimental results not only have important implications in understanding the mechanisms of crystallization and thermal stability in promising Fe–Si–B–P–Cu alloys, but also pave the way to tailor grain size and optimize soft magnetic properties for broad applications.

Author statement

Chenyu Lu: Investigation, Methodology, Writing - Original Draft. **Jiacheng Ge:** Investigation. **Si Lan:** Validation, Resources. **Xuelian Wu:** Investigation. **Zhenduo Wu:** Validation, Resources. **Lingxiang Shi:** Investigation. **Anding Wang:** Methodology. **Yan Zhang:** Methodology. **Chi Long Lai:** Investigation. **Kit Ying Leung:** Investigation. **Junhua Luan:** Methodology. **Elliot Paul Gilbert:** Investigation, Methodology. **Xun-Li Wang:** Supervision, Writing - Review & Editing

Declaration of competing interest

The authors declare that they have no known competing financial interests or personal relationships that could have appeared to influence the work reported in this paper.

Data availability

Data will be made available on request.

Acknowledgments

This work was supported by the National Natural Science Foundation of China (Nos. 51871120, 51571170, and 51501090). X.-L.W. acknowledges support from the Research Grants Council of Hong Kong Special Administrative Region (No. JLFS/P-102/18). X.-L.W., S.L. and Z. W acknowledge support by the Guangdong-Hong Kong-Macao Joint Laboratory for Neutron Scattering Science and Technology. S.L. acknowledges the support of the National Key R&D Program of China (No. 2021YFB3802800) and the Natural Science Foundation of Jiangsu Province (No. BK20200019). We acknowledge the support of the Australian Centre for Neutron Scattering, Australian Nuclear Science and Technology Organization, in providing the neutron scattering research facilities.

References

[1] J.M. Silveyra, E. Ferrara, D.L. Huber, T.C. Monson, Soft magnetic materials for a sustainable and electrified world, Science 362 (2018) 418, https://doi.org/10.1126/science.aao0195, 80-.
[2] G. Herzer, Modern soft magnets: amorphous and nanocrystalline materials, Acta Mater. 61 (2013) 718–734, https://doi.org/10.1016/j.actamat.2012.10.040.
[3] O. Gutfleisch, M.A. Willard, E. Brück, C.H. Chen, S.G. Sankar, J.P. Liu, Magnetic materials and devices for the 21st century: stronger, lighter, and more energy efficient, Adv. Mater. 23 (2011) 821–842, https://doi.org/10.1002/adma.201002180.
[4] C. Suryanarayana, A. Inoue, Iron-based bulk metallic glasses, Int. Mater. Rev. 58 (2013) 131–166, https://doi.org/10.1179/1743280412Y.0000000007.
[5] Y. Yoshizawa, S. Oguma, K. Yamauchi, New Fe-based soft magnetic alloys composed of ultrafine grain structure, J. Appl. Phys. 64 (1988) 6044–6046, https://doi.org/10.1063/1.342149.
[6] K. Hono, D.H. Ping, M. Ohnuma, H. Onodera, Cu clustering and Si partitioning in the early crystallization stage of an Fe73.5Si13.5B9Nb3Cu1 amorphous alloy, Acta Mater. 47 (1999) 997–1006, https://doi.org/10.1016/S1359-6454(98)00392-9.
[7] K.G. Pradeep, G. Herzer, P. Choi, D. Raabe, Atom probe tomography study of ultrahigh nanocrystallization rates in FeSiNbBCu soft magnetic amorphous alloys on rapid annealing, Acta Mater. 68 (2014) 295–309, https://doi.org/10.1016/j.actamat.2014.01.031.
[8] M. Ohnuma, K. Hono, S. Linderoth, J.S. Pedersen, Y. Yoshizawa, H. Onodera, Small-angle neutron scattering and differential scanning calorimetry studies on the copper clustering stage of Fe-Si-B-Nb-Cu nanocrystalline alloys, Acta Mater. 48 (2000) 4783–4790, https://doi.org/10.1016/S1359-6454(00)00277-9.
[9] A. Heinemann, H. Hermann, A. Wiedenmann, N. Mattern, K. Wetzig, A small-angle neutron scattering model for polydisperse spherical particles with diffusion zones and application to soft magnetic metallic glass, J. Appl. Crystallogr. 33 (2000) 1386–1392, https://doi.org/10.1107/S0021889800013248.
[10] X.D. Fan, H. Men, A.B. Ma, B.L. Shen, Soft magnetic properties in Fe 84-xB 10C 6Cu x nanocrystalline alloys, J. Magn. Magn Mater. 326 (2013) 22–27, https://doi.org/10.1016/j.jmmm.2012.08.045.
[11] R. Xiang, S.X. Zhou, B.S. Dong, G.Q. Zhang, Z.Z. Li, Y.G. Wang, The excellent soft magnetic properties and corrosion behaviour of nanocrystalline FePCCu alloys, J. Mater. Sci. Mater. Electron. 25 (2014) 2979–2984, https://doi.org/10.1007/s10854-014-1970-7.
[12] A. Wang, C. Zhao, H. Men, A. He, C. Chang, X. Wang, R.W. Li, Fe-based amorphous alloys for wide ribbon production with high Bs and outstanding amorphous forming ability, J. Alloys Compd. 630 (2015) 209–213, https://doi.org/10.1016/j.jallcom.2015.01.056.
[13] T. Liu, A. Wang, A. He, X. Wang, C.T. Liu, Y. Yang, Co-optimizing magnetic properties and thermal stability of high Bs nanocrystalline alloys with critical formability, J. Magn. Magn Mater. 487 (2019), 165310, https://doi.org/10.1016/j.jmmm.2019.165310.
[14] A. Makino, H. Men, T. Kubota, K. Yubuta, A. Inoue, New Fe-metalloids based nanocrystalline alloys with high Bs of 1.9 T and excellent magnetic softness, J. Appl. Phys. 105 (2009), 07A308, https://doi.org/10.1063/1.3058624.
[15] M. Matsuura, Y. Zhang, M. Nishijima, A. Makino, Role of P in nanocrystallization of Fe85Si2B8P4Cu1, IEEE Trans. Magn. 50 (2014) 2–5, https://doi.org/10.1109/TMAG.2013.2285247.
[16] H. Li, A. Wang, T. Liu, P. Chen, A. He, Q. Li, J. Luan, C.T. Liu, Design of Fe-based nanocrystalline alloys with superior magnetization and manufacturability, Mater. Today 42 (2021) 49–56, https://doi.org/10.1016/j.mattod.2020.09.030.
[17] K. Wood, J.P. Mata, C.J. Garvey, C.M. Wu, W.A. Hamilton, P. Abbeywick, D. Bartlett, F. Bartsch, P. Baxter, N. Booth, W. Brown, J. Christoforidis, D. Clowes, T. d'Adam, F. Darmann, M. Deura, S. Harrison, N. Hauser, G. Horton, D. Federici, F. Franceschini, P. Hanson, E. Imamovic, P. Imperia, M. Jones, S. Kennedy, S. Kim, T. Lam, W.T. Lee, M. Lesha, D. Mannicke, T. Noakes, S.R. Olsen, J.C. Osborn, D. Penny, M. Perry, S.A. Pullen, R.A. Robinson, J.C. Schulz, N. Xiong, E.P. Gilbert, QUOKKA, the pinhole small-angle neutron scattering instrument at the OPAL Research Reactor, Australia: design, performance, operation and scientific highlights, J. Appl. Crystallogr. 51 (2018) 294–314, https://doi.org/10.1107/S1600576718002534.
[18] S.R. Kline, Reduction and analysis of SANS and USANS data using IGOR Pro, J. Appl. Crystallogr. 39 (2006) 895–900, https://doi.org/10.1107/s0021889806035059.
[19] Y. Zhang, P. Sharma, A. Makino, Effects of cobalt addition in nanocrystalline Fe83.3Si4B8P4Cu0.7 soft magnetic alloy, IEEE Trans. Magn. 50 (2014) 8–11, https://doi.org/10.1109/TMAG.2013.2286617.

[20] A. Makino, T. Kubota, K. Yubuta, A. Inoue, A. Urata, H. Matsumoto, S. Yoshida, Low core losses and magnetic properties of Fe85-86Si 1-2B8P4Cu1 nanocrystalline alloys with high B for power applications (invited), J. Appl. Phys. 109 (2011) 4–9, https://doi.org/10.1063/1.3535169.
[21] P. Sharma, X. Zhang, Y. Zhang, A. Makino, Influence of microstructure on soft magnetic properties of low coreloss and high Bs Fe85Si2B8P 4Cu1 nanocrystalline alloy, J. Appl. Phys. 115 (2014) 2–5, https://doi.org/10.1063/1.4868188.
[22] C. Ioannidou, Z. Arechabaleta, A. Navarro-López, A. Rijkenberg, R.M. Dalgliesh, S. Kölling, V. Bliznuk, C. Pappas, J. Sietsma, A.A. van Well, S.E. Offerman, Interaction of precipitation with austenite-to-ferrite phase transformation in vanadium micro-alloyed steels, Acta Mater. 181 (2019) 10–24, https://doi.org/10.1016/j.actamat.2019.09.046.
[23] X. Xu, J. Odqvist, M.H. Colliander, S. King, M. Thuvander, A. Steuwer, P. Hedström, Effect of cooling rate after solution treatment on subsequent phase separation during aging of Fe-Cr alloys: a small-angle neutron scattering study, Acta Mater. 134 (2017) 221–229, https://doi.org/10.1016/j.actamat.2017.06.001.
[24] Y.Q. Wang, S.J. Clark, V. Janik, R.K. Heenan, D.A. Venero, K. Yan, D.G. McCartney, S. Sridhar, P.D. Lee, Investigating nano-precipitation in a V-containing HSLA steel using small angle neutron scattering, Acta Mater. 145 (2018) 84–96, https://doi.org/10.1016/j.actamat.2017.11.032.
[25] S.M. He, N.H. Van Dijk, M. Paladugu, H. Schut, J. Kohlbrecher, F.D. Tichelaar, S. Van Der Zwaag, In situ determination of aging precipitation in deformed Fe-Cu and Fe-Cu-B-N alloys by time-resolved small-angle neutron scattering, Phys. Rev. B Condens. Matter 82 (2010) 1–14, https://doi.org/10.1103/PhysRevB.82.174111.
[26] A. Guinier, G. Fournet, Small-Angle Scattering of X-Rays, John Wiley & Sons, New York, 1955.
[27] C. Wang, X. Guo, Y. Ivanisenko, S. Goel, H. Nirschl, H. Gleiter, H. Hahn, Atomic structure of Fe90Sc10 glassy nanoparticles and nanoglasses, Scripta Mater. 139 (2017) 9–12, https://doi.org/10.1016/j.scriptamat.2017.06.007.
[28] P. Sharma, X. Zhang, Y. Zhang, A. Makino, Competition driven nanocrystallization in high Bs and low coreloss Fe-Si-B-P-Cu soft magnetic alloys, Scripta Mater. 95 (2015) 3–6, https://doi.org/10.1016/j.scriptamat.2014.08.023.
[29] G. Porod, Die Röntgenkleinwinkelstreuung von dichtgepackten kolloiden Systemen - I. Teil, Kolloid Z. 124 (1951) 83–114, https://doi.org/10.1007/BF01512792.
[30] P.W. Schmidt, D. Avnir, D. Levy, A. Höhr, M. Steiner, A. Röll, Small-angle x-ray scattering from the surfaces of reversed-phase silicas: power-law scattering exponents of magnitudes greater than four, J. Chem. Phys. 94 (1991) 1474–1479, https://doi.org/10.1063/1.460006.
[31] Z.W. Zhang, L. Yao, X.L. Wang, M.K. Miller, Vacancy-controlled ultrastable nanoclusters in nanostructured ferritic alloys, Sci. Rep. 5 (2015) 1–9, https://doi.org/10.1038/srep10600.
[32] L. Yang, M.K. Miller, X.L. Wang, C.T. Liu, A.D. Stoica, D. Ma, J. Almer, D. Shi, Nanoscale solute partitioning in bulk metallic glasses, Adv. Mater. 21 (2009) 305–308, https://doi.org/10.1002/adma.200801183.
[33] L. Yang, X.L. Wang, A.D. Stoica, J. Almer, D. Shi, W.H. Wang, Multistage devitrification behavior of Mg 65 Cu 25 Tb 10 bulk metallic glass, Metall. Mater. Trans. A Phys. Metall. Mater. Sci. 39 (2008) 1947–1952, https://doi.org/10.1007/s11661-007-9415-z.
[34] F.R. de Boer, R. Boom, W.C.M. Mattens, A.R. Miedema, A.K. Niessen, Cohesion in Metals: Transition Metal Alloys, North Holland, New York, 1988.
[35] A. Takeuchi, A. Inoue, Classification of bulk metallic glasses by atomic size difference, heat of mixing and period of constituent elements and its application to characterization of the main alloying element, Mater. Trans. 46 (2005) 2817–2829, https://doi.org/10.2320/matertrans.46.2817.
[36] H. Okamoto, The Fe-P (iron-phosphorus) system, Bull. Alloy Phase Diagr. 11 (1990) 404–412, https://doi.org/10.1007/BF02843320.
[37] L. Hou, W. Yang, Q. Luo, X. Fan, H. Liu, B. Shen, High Bs of FePBCCu nanocrystalline alloys with excellent soft-magnetic properties, J. Non-Cryst. Solids 530 (2020), 119800, https://doi.org/10.1016/j.jnoncrysol.2019.119800.
[38] W. Yang, H. Liu, X. Fan, L. Xue, C. Dun, B. Shen, Enhanced glass forming ability of Fe-based amorphous alloys with minor Cu addition, J. Non-Cryst. Solids 419 (2015) 65–68, https://doi.org/10.1016/j.jnoncrysol.2015.03.035.
[39] Y. Wang, Y. Zhang, A. Takeuchi, A. Makino, Y. Kawazoe, Investigation on the crystallization mechanism difference between FINEMET® and NANOMET® type Fe-based soft magnetic amorphous alloys, J. Appl. Phys. 120 (2016), 145102, https://doi.org/10.1063/1.4964433.